DRAFT
CMS Paper

The content of this note is intended for CMS internal use and distribution only

Exploring small-angle emissions in charm jets in proton-proton collisions at $\sqrt{s} = 5.02$ TeV

The CMS Collaboration

Abstract

We present a measurement of the angular structure of jets containing a prompt D^0 meson and of inclusive jets in proton-proton (pp) collisions at the LHC at a center-of-mass energy of 5.02 TeV. The measurement uses collision data collected by the CMS experiment in 2017, corresponding to an integrated luminosity of 301 pb^{-1}. Two jet grooming algorithms, late-k_T and soft drop, are used to study the intrajet radiation pattern of these jets using the iterative Cambridge–Aachen declustering. The splitting angle distributions obtained with these two algorithms show that there is a shift of the distribution of prompt D^0 jets with respect to inclusive jets for jet transverse momentum of $100 < p_T^{jet} < 120$ GeV. The shift observed in late-k_T is consistent with the dead cone effect, whereas the shift for splittings selected with soft drop appears to be dominated by gluon splitting to charm quark-antiquark effects. The measured distributions are corrected to the particle level and set constraints on the substructure of high-p_T charm quark jets.

1 Introduction

The formation of jets, the highly collimated shower of hadrons produced in high-energy particle-particle colliders, is a rich multiscale process that probes different emergent phenomena of the strong interaction. Jet substructure techniques allow for an understanding of the jet shower formation as function of such momentum scales, allowing for the exposure of the building blocks of quantum chromodynamics (QCD). The radiation pattern of jets initiated by light quarks or gluons is governed by the infrarred and collinear divergences of QCD. For jets initiated by heavy quarks, such as charm or beauty quarks, these divergences are effectively regularized by the mass of the heavy quark, which leads to harder fragmentation of heavy-quark jets. This makes the jet showering process of heavy-quark jets distinct from those of light-quark jets, which is nontrivial to model with modern Monte Carlo (MC) event simulations when taking into account other effects, such as the modeling of the momentum recoil of the parton shower, color reconnection, and hadronization effects. Thus, measurements of heavy-quark jet substructure are needed in order to improve our understanding of final-state radiation with a mass scale.

The development of iterative jet declustering techniques has enabled the possibility of constructing a proxy for the parton branching process. A recent example is the direct observation of the dead cone effect in proton-proton (pp) collisions at the LHC [1]. The dead cone effect in QCD is the effect by which gluon emissions off a heavy quark are suppressed in a cone of angle $\theta_d = m_Q/E_Q$ around the emitting quark [2], where m_Q and E_Q are the mass and energy of the radiating heavy quark. It has been proposed, in addition, that the dead cone can potentially be used to understand medium-induced radiation in head-on heavy ion collisions, since it is expected to be a relatively clean environment. Thus, targeted measurements sensitive to the heavy-quark mass and how it affects the jet shower can provide inputs to improve the description of heavy-flavor jet showers. In this analysis, the primary focus is the substructure of charm quark jets, which are identified with the presence of a prompt D^0 meson contained in the jet.
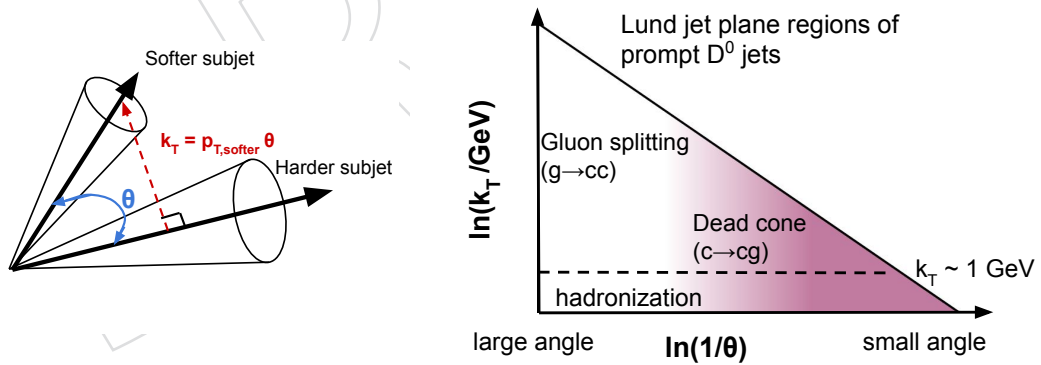

Figure 1: Left: Schematic diagram of two subjets, with their splitting angle θ and the relative transverse momentum k_T of the softer subjet with respect to the harder subjet. Right: Different Lund jet plane regions for charm quark jet showers. The vertical axis is the logarithm of the relative momentum k_T of the emission and θ the angle between the emission and the emitter. Gluon splitting to charm quark-antiquark pairs contribute primarily at large angles θ, hadronization effects contribute primarily to low $k_T < 1\,\mathrm{GeV}$ and the dead cone effect is located at small angles.

The iterative declustering of an angular-ordered jet tree allows the kinematic properties and mass effects at the level of an individual emission to be accessed. In an angular-ordered tree, such as the one obtained with Cambridge–Aachen (CA) [3] pairwise clustering algorithm, the

splittings that are clustered first are those that have the smallest angular separations, where mass effects are the strongest. The dead cone angle is different for each splitting, since it depends on the energy of the mother branching. Using the CA tree, one can map out the kinematics of the intrajet radiation in terms of the Lund jet plane representation, as shown in Fig. 1. In Fig. 1, on the left panel we give a schematic representation of two subjets, annotating the splitting angle θ and relative transverse momentum k_T between them. In this two-dimensional plane, the phase space of $1 \rightarrow 2$ splittings obtained from the CA tree can be visualized, where the vertical axis corresponds to the logarithm of the relative transverse momentum of the emission relative to the emitter, k_T, and the rapidity–azimuth splitting angle θ of the branching, as shown on the right panel in Fig. 1.

The Lund jet plane enables the visualization of the jet shower in a modular fashion. For instance, one can separate the hadronization and parton showering using a selection in k_T, corresponding to a horizontal line in the Lund jet plane. It also allows for isolating angular regions of interest from one another. The different Lund jet plane regions for prompt D^0 jets can be seen in Fig. 1.

In Refs. [4], two elements were identified as being key to the direct exposure of the dead cone:

- The decays of the heavy-flavor hadrons create additional small-angle splittings in the jet clustering tree, such that the dead cone is filled by them. One way to overcome this issue is to select jets with fully reconstructed heavy-flavor hadrons in them.
- Hadronization effects need to be suppressed. This can be achieved by imposing a k_T cutoff on the splittings, where the k_T cutoff is larger than the hadronization scale.

The ALICE Collaboration used the Lund jet tree for the direct evidence of the dead cone effect in jets containing a fully reconstructed D^0 meson [1]. To further extend the exploration of the dead cone effect of QCD, in a way such that it can be approachable by first principles calculations and to reduce the dimensionality of the corrections to the particle level, an alternative strategy needs to be followed.

In this analysis, a different approach is followed in order to expose mass effects in heavy-flavor quark jets, such that it facilitates the interpretation of the data for pp and lead-lead collisions. The strategy consists of selecting one emission per jet. The specific types of emissions are selected by applying a recently proposed grooming algorithm known as "late-k_T" [5], designed to select hard and collinear emissions. This algorithm selects the last splitting in the CA jet tree with a k_T value larger than some threshold of choice, preferably larger than $\Lambda_{QCD} \approx 200\,\text{MeV}$. In this way, the sensitivity to charm quark mass effects is enhanced and the sensitivity to hadronization effects and to direct contributions from gluon splitting to charm quark-antiquark pairs is strongly suppressed (g$\rightarrow$ cc).

We also consider a modified version of the soft drop grooming algorithm (SD) [6, 7] with a k_T selection imposed such that hadronization effects are minimized. The emissions selected with the SD algorithm are typically found at larger angles than the ones selected with the late-k_T algorithm. Thus, the SD emissions are potentially more sensitive to effects like gluon splitting to charm quark-antiquark pair or the underlying event activity. Comparing the resulting angular distributions obtained with these two algorithms exposes a modification of the angular scale in D^0 jets relative to inclusive jets in a regime of high jet p_T. Other measurements of groomed jet substructure of D^0 jets exist at the LHC [8], where the fragmentation of D^0 jets is constrained at a lower jet p_T.

In this analysis, we focus on high-p_T jets, with a p_T of at least $100\,\text{GeV}$. This minimum p_T allows for a description in the framework of perturbation theory, while still allowing for the

visualization of a sizeable impact of the dead cone effect. The measurement is performed using (pp) data recorded by the CMS detector, whose components are described in Section 2, which also describes the algorithms used to reconstruct events, jets, and D^0 mesons. This section also contains details of the measured and simulated samples. Details of analysis steps for both inclusive and prompt D^0 jets and chain of corrections that are applied are described in Section 3. The strategy for the corrections to stable-particle level is discussed in Section 4. The systematic uncertainties in the corrected distributions are described in Section 5. The corrected distributions and their comparison with theoretical calculations are reported in Section 6. A summary of the measurement is presented in Section 7.

2   The CMS detector, event reconstruction, and samples description

The analysis uses pp data collected by the CMS experiment in 2017 at a center-of-mass energy of 5.02 TeV, which corresponds to an integrated luminosity of $301 \pm 6 \, \text{pb}^{-1}$ [9].

The CMS apparatus [10, 11] is a multipurpose, nearly hermetic detector, designed to trigger on [12, 13] and identify electrons, muons, photons, and (charged and neutral) hadrons [14–16]. A global "particle-flow" (PF) algorithm [17] aims to reconstruct all individual particles in an event, combining information provided by the all-silicon inner tracker and by the crystal electromagnetic (ECAL) and brass-scintillator hadron calorimeters (HCAL), operating inside a 3.8 T superconducting solenoid, with data from the gas-ionization muon detectors embedded in the flux-return yoke outside the solenoid. The reconstructed particles are used to build τ leptons, jets, and missing transverse momentum [18–20].

Events of interest are selected using a two-tiered trigger system. The first level (L1), composed of custom hardware processors, uses information from the calorimeters and muon detectors to select events at a rate of around 100 kHz for pp collisions [12]. The second level, known as the high-level trigger (HLT), consists of a farm of processors running a version of the full event reconstruction software optimized for fast processing and reduces the event rate to around 1 kHz before data storage [13].

The average pileup activity during data taking was two interactions per bunch crossing. The low-pileup activity facilitates the use of neutral hadron PF candidates for the substructure measurement, which ease the comparison of the observable to calculation.

The events are required to have a primary vertex reconstructed within 15 cm of the nominal interaction point along the beam direction, and within 0.15 cm in the transverse plane. The additional collisions per bunch crossing have a negligible effect on the measurement.

Events with high-p_T jets are collected with triggers requiring at least one calorimeter jet with energy above 60 and 80 GeV. The trigger has an efficiency of 92% for PF jets of 80 GeV and of 99% at 100 GeV. The trigger inefficiencies are simulated in dedicated Monte Carlo samples. The differences in the trigger efficiency based on data-to-simulation comparisons are corrected as a function of the jet p_T.

Jets are clustered from the list of PF candidates using the anti-k_T algorithm [21, 22] with a distance parameter $R = 0.2$. The choice of using small jet radius is convenient since this measurement is intended to be a reference for future heavy ion collision measurements where small-R is a common choice to mitigate the impact of uncorrelated background contributions, at the level of jet momentum and substructure [23]. Moreover, our focus is the small-angle region of the intrajet radiation pattern which is the most sensitive to quark mass effects.

The four-momentum of the jet is determined using the vector sum of all particle momenta in the jet. For this analysis, jets are required to have $80 < p_T^{\text{jet}} < 160\,\text{GeV}$ and pseudorapidity $|\eta| < 1.6$. The selection of jets at central pseudorapidities is driven by the choice of the D^0 meson candidate selection described in the next paragraph, which is primarily at central pseudorapidities. The jets are corrected for the detector response with jet energy corrections derived from independent pp simulations along with additional corrections for the imperfect modeling of the detector response [24]. In addition to the jet energy correction, the momentum resolution of jets is larger in data than in simulation. Corrections to the simulation to account for the momentum resolution differences are derived from dijet balancing studies [19]. To incorporate this effect, a Gaussian smearing is applied to the detector-level jet p_T values in simulation to match the resolution in data.

The D^0 meson candidates are reconstructed by combining pairs of oppositely-charged particle tracks with an invariant mass within ± 0.2 GeV of the world-average D^0 meson mass, $1.86\,\text{GeV}$ [25]. For the computation of the D^0 meson mass, it is assumed that one of the charged particles is a kaon and the other a pion. To suppress the contribution of combinatorial background, each track is required to have a $p_T > 1\,\text{GeV}$, to be within $|\eta| < 2.4$, and to satisfy a set of track quality selection requirements. Each D^0 meson candidate is selected with a $p_T > 4\,\text{GeV}$ and $|y| < 1.2$. The jets that have at least a D^0 candidate at a distance from the jet axis smaller than the jet radius R, are tagged as D^0-jets. The invariant mass of such D^0 candidates that are geometrically matched to jets, is recorded in bins of the jet splitting angle and jet momentum. To optimize the D^0 meson signal significance, additional selection requirements are applied to the D^0 candidates. A cut-based approach is followed, where the selection is optimized using binary trees to maximize the signal significance squared [26], ranging from 10 to about 30. The signals at the particle level are prompt D^0 mesons as given by the simulation. The detector-level variables used in the optimization are related to the topology of the secondary vertex: the distance between primary and secondary vertices (d_0) normalized by its uncertainty in the direction transverse to the beam, the angle between the total momentum vector of the daughter tracks and the vector connecting the primary and the secondary vertices (pointing angle α), the secondary vertex probability and the significance of the distance of the closest approach (DCA). Out of the sample of two million jets with $100 < p_T < 120\,\text{GeV}$, about 25 thousand of them are found to have at least one D^0 meson candidate in data with the characteristics described here.

The minimum p_T of the D^0 mesons used in the analysis is $4\,\text{GeV}$. This selection requirement is used to suppress the large combinatorial background in D^0 reconstruction in the heavy ion environment, for which the present measurement is used as a baseline. A higher D^0 p_T requirement also helps mitigate possible data-to-simulation differences in the reconstruction efficiency of the D^0 meson, as well as a reduction of the combinatorial background from random hadron-hadron pairings. Based on MC simulation studies, the D^0 p_T threshold does not introduce a bias in the jet substructure distributions presented in this paper. The same minimum p_T for the D^0 of $4\,\text{GeV}$ is used for the corrections to the particle level, i.e., there is no p_T acceptance correction for the D^0 meson p_T. A correction for the single-particle p_T acceptance is applied to the decay daughters of the D^0 meson.

The PYTHIA 8.230 [27] event generator with tune CP5 [28] is used to derive MC corrections and for making comparisons with the data. For the pp simulated events, a second sample is generated at leading-order (LO) in perturbation theory using the HERWIG 7.2.2 [29–31] generator with the CH3 tune [32]. This second sample is used to assess systematic uncertainties related to the modeling of the parton shower, hadronization, multiparton interactions, and beam-beam remnant interactions. These generated samples are passed through a detailed simulation of the CMS detector using GEANT4 [33]. Additional particle-level predictions are compared with

168 the corrected distributions. Predictions are computed at LO with PYTHIA8.303 with the CP5
169 tune [28, 34, 35].

170 The observables considered in this analysis are reported at the particle level. To estimate the
171 impact of hadronization effects, we have computed the angular distributions at parton and
172 stable-hadron levels using both PYTHIA8 CP5 and HERWIG7 CH3 generators. For a given MC-
173 generated event, the list of partons and stable hadrons is analyzed simultaneously. At hadron
174 level, prompt D^0 jets are selected with the same kinematic selection requirements on the jets,
175 the substructure, and the D^0 meson in the jet. At parton level, jets are required to have a charm
176 quark as a constituent (since there is no D^0 meson), and the CA reclustering is performed over
177 the list of partons as provided by the respective MC generator. Only parton- and hadron-level
178 jets that are matched geometrically are used for this comparison. Hadronization effects are
179 quantified through the bin-by-bin difference between the hadron-level jet substructure observ-
180 able and the substructure of the matched parton-level jet. Hadronization effects are of the order
181 of 10% across the whole angular range for both late-k_T and soft drop grooming, demonstrating
182 the resilience of these observables to hadronization effects.

183 # 3 Analysis method

184 This analysis reports the angular distribution of the intrajet emissions in two different regions
185 of the Lund plane for jets containing a prompt D^0 meson and inclusive jets, as selected by
186 two grooming algorithms, the late-k_T and a modified version of the soft drop algorithm, as
187 described next.

188 First, the anti-k_T jets [21, 22] are reclustered using the CA algorithm, which is a pairwise clus-
189 tering algorithm that clusters particles (and subjets thereafter) that are closer in rapidity and
190 azimuth, imposing angular ordering [3, 36]. The PF candidates with $p_T > 1\,\text{GeV}$ of the original
191 anti-k_T jet are used for the CA reclustering step, which includes neutral and charged PF candi-
192 dates. The $p_T > 1\,\text{GeV}$ threshold is applied to avoid the fast drop of the track reconstruction
193 efficiency and reduce data-to-simulation differences.

194 Then, the CA pairwise clustering history is then followed in reverse. Starting with the reclus-
195 tered jet, the last step of the CA clustering is undone, such that the original jet is "declustered"
196 into the two subjets of the previous clustering step. This procedure is performed iteratively,
197 declustering the harder subjet at each step of the iteration. Jet grooming consists of selecting a
198 specific pair of subjets from this iterative CA declustering procedure.

199 The late-k_T grooming algorithm selects the last pair of subjets that satisfies the $k_T > 1\,\text{GeV}$
200 selection, where $k_T = \theta p_T^{\text{sub}}$, and p_T^{sub} is the transverse momentum of the subleading subjet at
201 the respective declustering step. In addition, for D^0 jets it is required that the D^0 meson is a
202 constituent of the harder subjet in the selected pair of subjets. The late-k_T algorithm scans the
203 region of collinear and hard emissions in the Lund jet plane.

204 The default soft drop grooming algorithm selects the first pair of CA subjets that satisfies the
205 condition $z > z_{\text{cut}}\theta^\beta$. Here, z corresponds to the momentum fraction $z = p_T^{\text{sub}} / (p_T^{\text{sub}} + p_T^{\text{lead}})$
206 where p_T^{lead} (p_T^{sub}) is the momentum of the harder (softer) subjet in the declustering step and θ
207 the distance in y–ϕ between the harder and softer subjets in the declustering procedure. In this
208 modified version of the soft drop algorithm, we select the first splitting that satisfies the two
209 requirements: $z > z_{\text{cut}}\theta^\beta$ and $k_T > 1\,\text{GeV}$. The parameters are set to $z_{\text{cut}} = 0.1$ and $\beta = 0$, which
210 facilitates the comparison with theoretical calculations [37]. The additional k_T requirement is
211 applied to reduce the sensitivity to hadronization effects at small angles, thereby improving

6

the correspondence between the parton- and hadron-level predictions.

The angle between the softer and harder subjets selected by the late-k_T or the modified SD grooming algorithm, denoted by θ_l or θ_{SD}, respectively, is the main observable reported in this measurement. The present analysis reports such splitting angle distributions for jets containing a prompt D^0 meson (prompt D^0 jets) jets and for inclusive jets. The inclusive jet sample is dominated by light-quark and gluon jets.

Our results are reported in $100 < p_\mathrm{T}^\mathrm{jet} < 120\,\mathrm{GeV}$, where our jet triggers sampled nearly the full luminosity. A fixed jet p_T window is chosen to limit smearing of the dead cone region, as the effect depends on the jet p_T.

The analysis workflow for D^0 jets can be summarized by the following steps. The D^0 meson candidates are reconstructed, as described previously. The two charged-particle track daughter candidates are combined to form the D^0 meson candidate four-momentum. This D^0 meson candidate replaces the two daughters, which are removed from the list of particles that are used as input for the jet finding. The jet substructure observables are computed using the jets that contain at least a D^0 meson candidate as a constituent. The reconstructed jet p_T is in the range $80 < p_\mathrm{T}^\mathrm{jet} < 160\,\mathrm{GeV}$. The D^0 meson yield in each jet p_T and θ_l (θ_{SD}) bin is extracted with a binned maximum likelihood fit to the invariant mass distributions of the D^0 candidate in the range $[1.7, 2.0]\,\mathrm{GeV}$. The signal shape is modeled as the sum of two Gaussian functions with the same mean but different widths. The combinatorial background originating from random pairs of tracks is modeled with a third-order polynomial function. An additional Gaussian function with a larger width is used to model the invariant mass distribution of D^0 meson candidates that result from the incorrect mass assignment for the pion and kaon tracks. Backgrounds from decays $\mathrm{D}^0 \to \mathrm{K}^+\mathrm{K}^-$ and $\mathrm{D}^0 \to \pi^+\pi^-$ are modeled with Crystal Ball functions. Examples of such fits are shown in Fig. 2.
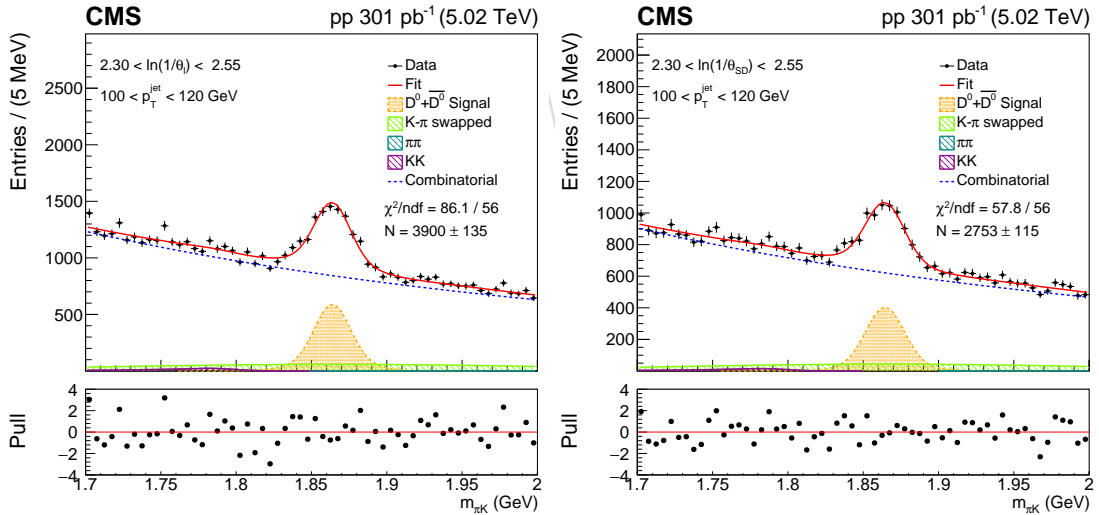

Figure 2: Invariant mass distribution of particle pairs for D-jet candidates and fits for late-k_T (left) and modified soft drop (right) for splitting angle and jet momentum in the range: $2.3 < \theta_l(\theta_{\mathrm{SD}}) < 2.55$ and $100 < p_\mathrm{T}^\mathrm{jet} < 120\,\mathrm{GeV}$.

It is likely that the clustering of a pair of particles with a combined $p_\mathrm{T} > 4\,\mathrm{GeV}$ and with an invariant mass compatible with the D^0 meson could sculpt the jet substructure distribution such that it mimics the sought dead cone effect. In order to test this, we performed a check using the low- and high-mass sidebands around the D^0 candidates instead of selecting the

D^0 candidates, with the same $p_T > 4\,\text{GeV}$ selection. The pair of tracks is replaced by such a sideband-D^0 candidate. The substructure of such sideband-D^0 jets is found to be compatible with the inclusive jet baseline, showing that there are no significant kinematical biases, as seen in Fig. 3.

To subtract the nonprompt D^0 meson contributions, we perform a sideband subtraction method using the DCA significance distribution, which allows for the separation of the nonprompt and prompt D^0 meson contributions in the extremes of the distribution. Nonprompt D^0 mesons are those D^0 mesons that do not originate from the fragmentation of a charm quark but that come from decays of beauty hadrons. In this case, the reconstructed jet will contain the D^0 meson and other particles from the b hadron decay as constituents.

These other decay products may create extra splittings in the CA declustering, leading to contamination in the collinear region of interest. In Fig. 4, left panel, we show the detector-level DCA significance distribution fitted with PYTHIA8 CP5 templates for prompt and nonprompt D^0 mesons contained in jets. The nonprompt and prompt D^0 templates derived from HERWIG7 CH3 simulated samples are compatible in shape with the ones derived from PYTHIA8. The plot on the right shows the D^0 jet substructure distribution and nonprompt D^0 meson contribution obtained with fits in bins of DCA, splitting angle, and jet p_T. The nonprompt D^0 meson contribution is found to be around 15%. The nonprompt D^0 subtraction causes a reduction of the uncorrected yield and a change in the shape of the substructure. We also keep track of the number of jets that have not satisfied grooming criteria and in the case of D^0 jets it is 30-40% (for inclusive jets this fraction is around 25%).

To account for migration effects due to detector resolution effects, we correct to the particle level the prompt D^0 jet substructure. This correction is a two-dimensional unfolding where we unfold simultaneously the jet p_T and the splitting angle of interest (either θ_l or θ_{SD}). The same p_T selections on particles are applied at detector and particle level, including the $4\,\text{GeV}$ cutoff on the D^0 meson p_T. Finally, we correct the unfolded result by the selection, acceptance, and reconstruction efficiency of the prompt D^0 mesons. The efficiency correction factor is of the order of 50% and has a weak dependence on the splitting angle. This emphasizes the fact that decay properties on which we base our D^0 selection are uncorrelated to the jet substructure. The procedure is detailed in the next section. To reduce data-to-simulation differences in the jet energy calibration for prompt D^0 jets, the ratio distribution of the D^0 and jet momentum in the detector level simulation is reweighted to match the data distribution.

4 Corrections to the particle level

The measured detector-level distributions are corrected to the stable particle level using corrections derived from the simulation. The particle level is defined by the set of particles that have a lifetime longer than $10^{-8}\,\text{s}$ as given by the MC event generator. For the simulated prompt D^0 jet signal events, the D^0 mesons replace the kaon and pion daughters before the jet reclustering, analogous to what is done at detector level. The D^0 meson replacement at particle level uses generator-level information for the mother-daughter association. For the inclusive jet corrections, such a replacement is not performed. First, a set of bin-by-bin corrections is applied to the detector-level distribution to account for the background (purity corrections). In this measurement, the background consists of detector-level emissions that are not paired with particle-level emissions. Then, to correct for bin-to-bin migrations due to detector effects, a two-dimensional unfolding of the jet p_T and the angular variable of interest is applied. After the correction for bin-to-bin migration effects, a set of bin-by-bin corrections to account for particle-level emissions that are not reconstructed at the detector level (efficiency corrections)
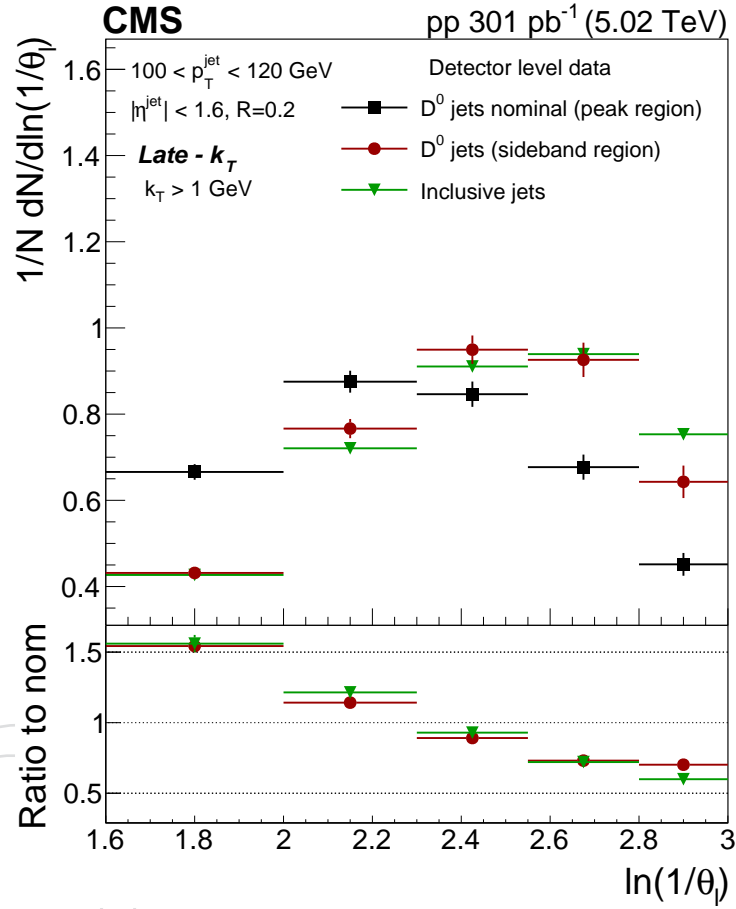
Figure 3: Comparison of the $\ln(1/\theta_l)$ distributions for different windows of the invariant mass of the track pairs and the inclusive jets selection. The black rectangles represent the selection for D^0 meson candidates in the resonance region (dominated by signal D^0 meson candidates), the red circles represent D^0 meson candidates from the mass sideband region (dominated by combinatorial background), and green triangles represent the inclusive jet. In the lower panel, a ratio to nominal signal is shown. The error bands represent the statistical uncertainties.
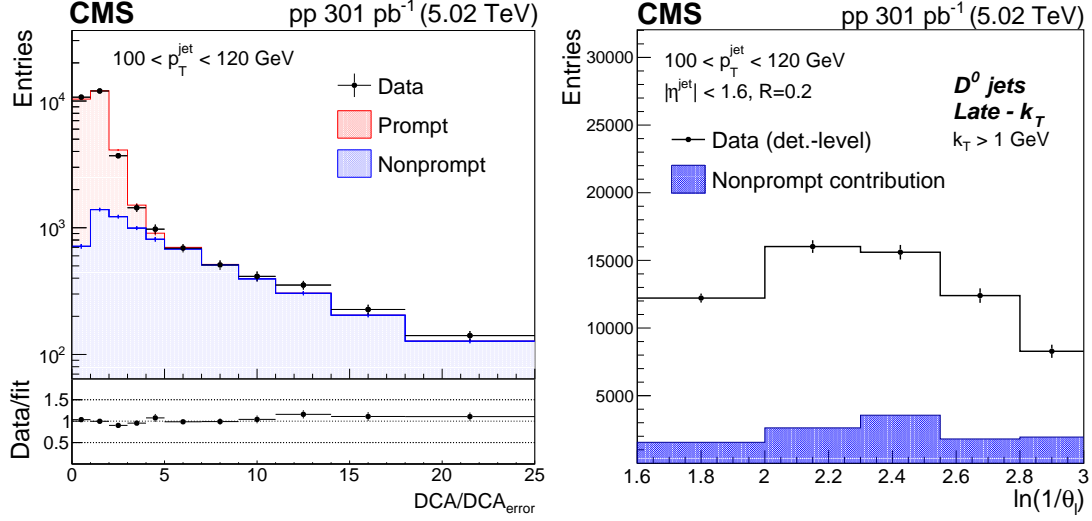
Figure 4: Left: Detector-level DCA significance distribution in data fitted with PYTHIA8 CP5 templates for prompt and nonprompt D^0 mesons contained in jets. In the lower panel, the ratio between the data and the fit values is presented. Right: Measured D^0 meson yields (black circles) and nonprompt D^0 meson contribution (filled histogram) as a function of the late-k_T splitting angle θ_l.

is applied. At particle and detector levels, jets are clustered with a $p_T > 1\,\text{GeV}$ requirement on the particles used for the jet CA reclustering (with the exception of the D^0 meson in the case of the D^0 jet analysis, where an additional selection of D^0 $p_T > 4\,\text{GeV}$ is required). The particle-level distribution shares the same binning as the detector-level distribution, and in addition has overflow and underflow bin to account for out-of-phase migrations in the unfolding procedure. The particle-level distributions have additional underflow and overflow bins to account for phase space migrations, which are removed after the full chain of corrections.

To derive the corrections, a mapping between the detector- and particle-level emissions is necessary. If the particle- and detector-level jets satisfy the grooming criteria, the splittings selected at particle- and detector-level are required to be, in addition, the closest in proximity among all the primary emissions in the detector- and particle-level CA trees. The cases where the mapping criteria are not satisfied are accounted for via purity and efficiency corrections.

A two-dimensional unfolding is performed to correct for the bin-to-bin migrations caused by detector effects. The dimensions that are considered in the correction are the anti-k_T jet p_T and the splitting angle (θ_l or θ_{SD}). Two separate two-dimensional unfolding procedures are performed. Unfolding with direct matrix inversion yields large bin-to-bin oscillations in the unfolded distributions. Therefore, we perform the regularized matrix inversion using iterative D'Agostini unfolding with early stopping [38]. We use its implementation in the ROOUNFOLD package [39].

The number of iterations plays the role of the regularization parameter in iterative D'Agostini unfolding. A value for the number of iterations must be chosen. In this analysis, we choose the number of iterations based on χ^2 goodness-of-fits tests at detector level. At each iteration of D'Agostini unfolding performed using PYTHIA8 CP5, the unfolded distribution is mapped back to the detector level by matrix multiplication using the same migration matrix. We call this process "forward folding," and the detector-level distribution obtained after matrix multiplication as the "forward-folded distribution." To quantify the compatibility between the forward-folded distribution and the input-measured distribution, the χ^2 of the forward-folded

distribution and the measured detector-level distribution are calculated at a given iteration. By construction of the D'Agostini unfolding algorithm, the agreement between the input distribution and the forward-folded distributions improves monotonically at each iteration. To avoid overfitting the unfolded distribution to the statistical fluctuations present in the measured distributions, the unfolding algorithm is stopped at the iteration at which the corresponding p-value is above 0.99.

The corrections are derived using PYTHIA8 CP5 and HERWIG7 CH3 simulated events. Neither of the detector-level predictions of PYTHIA8 CP5 and HERWIG7 CH3 can describe the data in the entire distribution. The nominal set of corrections is derived using the sample of PYTHIA8 CP5 simulated events. The sample of HERWIG7 CH3 simulated events is used to estimate biases in the unfolding corrections and to compute the systematic uncertainties associated with the model dependence of the corrections, as described in Section 5.

5 Systematic uncertainties

The experimental uncertainties are propagated by repeating the unfolding procedure with variations of the response matrix, prior distribution, purity, and efficiency corrections. The following systematic uncertainties are considered:

Jet energy scale and resolution: The jet energy scale uncertainty is propagated through the unfolding by shifting the jet p_T at detector level in the simulation according to the η–p_T dependent jet energy scale uncertainties [19]. This uncertainty has an effect through the $80 < p_T^{jet} < 160\,\text{GeV}$ selection requirement. The uncertainty is smaller than 7% (3%) throughout the unfolded angular distributions for D^0 jets (inclusive jets). We also consider the uncertainties in the jet energy resolution measurement [19]. The jet p_T is further smeared at detector level in simulation to better reproduce the jet energy resolution measured in data [19]. Such a smearing procedure comes with an associated systematic uncertainty, which is propagated through the unfolding procedure.

PF candidate energy scale: For a given anti-k_T jet, the four momenta of the jet constituents are shifted by 1% for charged particles, 5% for neutral hadrons, and 3% for photons [17, 19, 40]. With these variations, the impact of the individual calibration of PF candidate is estimated. The variations are done independently for each PF candidate type, treating the up and down variations as uncorrelated. This corresponds to six different variations.

Tracking efficiency: To account for the mismodeling of track reconstruction in the simulation we propagate a track reconstruction efficiency uncertainty through the unfolding procedure. This is done by randomly removing 3% of the tracks in the simulation. The tracking efficiency has two effects in this analysis. One of them is at the substructure level, whereas the other has to do with the reconstruction of the D^0 meson candidate. The D^0 meson reconstruction relies on charge-particle tracks and the removal of 3% of the tracks is done before the D^0 meson candidate reconstruction. The jet substructure is calculated using all PF candidate species. Rather than losing the PF candidate, as it would happen in a charged-only jet substructure measurement, we assume that the charged hadron is reconstructed instead as a neutral hadron, and its energy is smeared by 10% due to the hadronic calorimeter resolution. The tracking efficiency uncertainty is propagated through the whole chain of corrections in a correlated way, affecting the D^0 meson reconstruction efficiency, response matrix through the energy resmearing of the charged-particle PF candidates that are "lost" in the reconstruction from this variation, as well as the MC-based template fits that are used for the nonprompt D^0 meson background subtraction. The dominant effect is the reduction of the D^0 reconstruction efficiency. This systematic

uncertainty is symmetrized bin-by-bin for both D^0 and inclusive jet substructure distributions.

Physics model uncertainty: The choice of the physics model impacts the unfolding corrections of the measured observable via the description of the jet showering pattern, which changes the detector response at the subjet level, as well as the prior spectrum used for regularization. The model uncertainty is constructed by using HERWIG7 CH3 generated events instead of PYTHIA8 CP5 for the prior spectrum, the migration matrix, and the matching purity and efficiency.

Response matrix statistical uncertainties: The statistical uncertainties of the simulated sample that is used to derive the migration matrix are propagated through the unfolding procedure, which results in a contribution to the covariance matrix.

Signal extraction and background modeling: The D^0 yield extraction is performed using a triple Gaussian function, instead of the nominal double Gaussian function used by default. The variation is made to take into account possible deviations in the shape for the nominal configuration. The uncertainty associated with the modeling of the combinatorial background is estimated by using an exponential function and a second-order polynomial instead of the nominal approach of using a third-order polynomial.

Prompt D^0 meson fraction: Nominally, the prompt D^0 meson fraction is determined via template fits of prompt and nonprompt D^0 meson production using the DCA significance distribution. To avoid possible detector simulation biases on the DCA significance variable, we use an alternative method for the prompt D^0 meson extraction based only on the DCA distribution. A correction to the detector-level DCA in simulation is applied in order to improve the DCA resolution, following the method described in Ref. [41]. The template fits based on the DCA distribution are repeated after this correction, leading to uncertainty in the prompt D^0 meson fraction with respect to the nominal DCA significance method.

Regularization bias: The optimal number of iterations in the D'Agostini method depends on the initial particle-level spectrum. To gauge the dependence on the initial spectrum, the unfolding of the data using a PYTHIA8 CP5 response is repeated for the optimal number of iterations found when unfolding data with a HERWIG7 CH3 response.

Fit function modeling of trigger scale factor: The trigger efficiencies in data and MC are fitted with an error function parametrization instead of the nominal logistic function used as default. The correction chain is repeated with this modification, and the difference relative to the nominal choice is used to quantify this systematic uncertainty.

The resulting relative systematic uncertainties on the normalized jet substructure distributions are summarized in Table 1. The dominant systematic uncertainties are the JEC and the PF scale uncertainties.

Uncertainties with a two-point variation, such as the jet energy scale uncertainty, are symmetrized bin-by-bin. The one-sided variations are kept as one-sided, with the exception of the tracking efficiency uncertainty, which is symmetrized bin-by-bin. The different sources of uncertainty are considered to be independent from each other and their effects are added in quadrature at a given bin. The systematic uncertainties of each source are considered as bin-to-bin fully correlated. The tracking efficiency, PF candidate energy scale, trigger fit modeling, and jet energy resolution uncertainties are propagated as fully correlated bin-by-bin in the D^0-to-inclusive jet ratio presented in the next section. Other systematic uncertainties, such as those specific to the prompt D^0 jet analysis, are propagated as uncorrelated in the D^0-to-inclusive jet ratio. The jet energy scale uncertainty and physics model are propagated as uncorrelated in the ratio of D^0-to-inclusive jet distributions. The statistical correlation between the D^0 jet and the

inclusive jet sample is taken into account in the propagation of the statistical uncertainties for the ratio, which results in a statistical correlation coefficient of a few percent.

Table 1: Summary of percentual relative uncertainties.

Uncertainty source	Late-k_T		Soft drop	
	Prompt D^0 jets	Inclusive jets	Prompt D^0 jets	Inclusive jets
Jet energy scale	1.5–5.8%	0.3–2.6%	0.7–4.6%	0.2–2.4%
Jet energy resolution	0.3–1.4%	0.3–0.9%	0.6–1.5%	0.2–0.8%
Charged hadron PF energy scale	0.2–0.6%	0.7–1.4%	0.2–0.8%	0.4–0.8%
Neutral hadron PF energy scale	1.3–2.8%	0.3–1.3%	1.4–5.3%	0.1–1.5%
Photon PF energy scale	0.3–1%	0.5–6%	0.2–1%	0.1–0.8%
Tracking efficiency	0.3–1.2%	0.1–0.5%	0.2–2.5%	0.03–0.3%
Physics model dependence	0.6–5.4%	0.4–2.8%	2.3–7.2%	0.8–3%
Response matrix statistical	5.5–9.6%	0.9–1.5%	5.2–14.9%	0.6–1.2%
Signal extraction	0.1–0.6%	—	0.02 -0.2%	—
Background modeling	0.5–2.8%	—	2.3–7.6%	—
Prompt D^0 fraction	0.7–3.8%	—	2.4–12.8%	—
Regularization bias	0.4–2.9%	0.3-0.7%	0.4–3.5%	0.1–0.9%
Trigger scale factor	$\leq 0.02\%$	$\leq 0.02\%$	$\leq 0.03\%$	$\leq 0.02\%$
Statistical	6.5–11.7%	1.1–1.7%	7.1–20%	0.8–1.4%

6 Results

In Figs. 5 and 6, the corrected θ_l and θ_{SD} distributions are presented for prompt D^0 jets and inclusive jets. The distributions are normalized to the number of jets that satisfy the respective grooming criteria. The distributions are compared to PYTHIA8 CP5 and HERWIG7 CH3 at particle-level. These predictions are in agreement with the measured θ_l and θ_{SD} distributions of the prompt D^0 jet measurement within the experimental uncertainties. Concerning the distributions for inclusive jets, HERWIG7 CH3 describes the data better than PYTHIA8 CP5, consistent with other jet substructure measurements in inclusive jets [42, 43]. The PYTHIA8 CP5 and HERWIG7 CH3 predictions are consistent with each other for D^0 jets, and the differences between them are larger for inclusive jet production, which is dominated by light-quark and gluon jets.

In Fig. 7, the D^0 jet and the inclusive jet distributions are presented, as well as the ratio of the D^0 jet distribution with respect to the inclusive jet one. The D^0 jet angular distributions are effectively "shifted" towards larger splitting angles relative to the inclusive jet distributions, consistent with the dead cone effect expectation. The shift with respect to the inclusive jet distribution is stronger for the late-k_T angle distribution than for the modified SD one. The HERWIG7 CH3 generator describes the ratio of D^0 jet to inclusive jet better, which is mostly because HERWIG7 CH3 describes the inclusive jet distribution better than PYTHIA8 CP5.
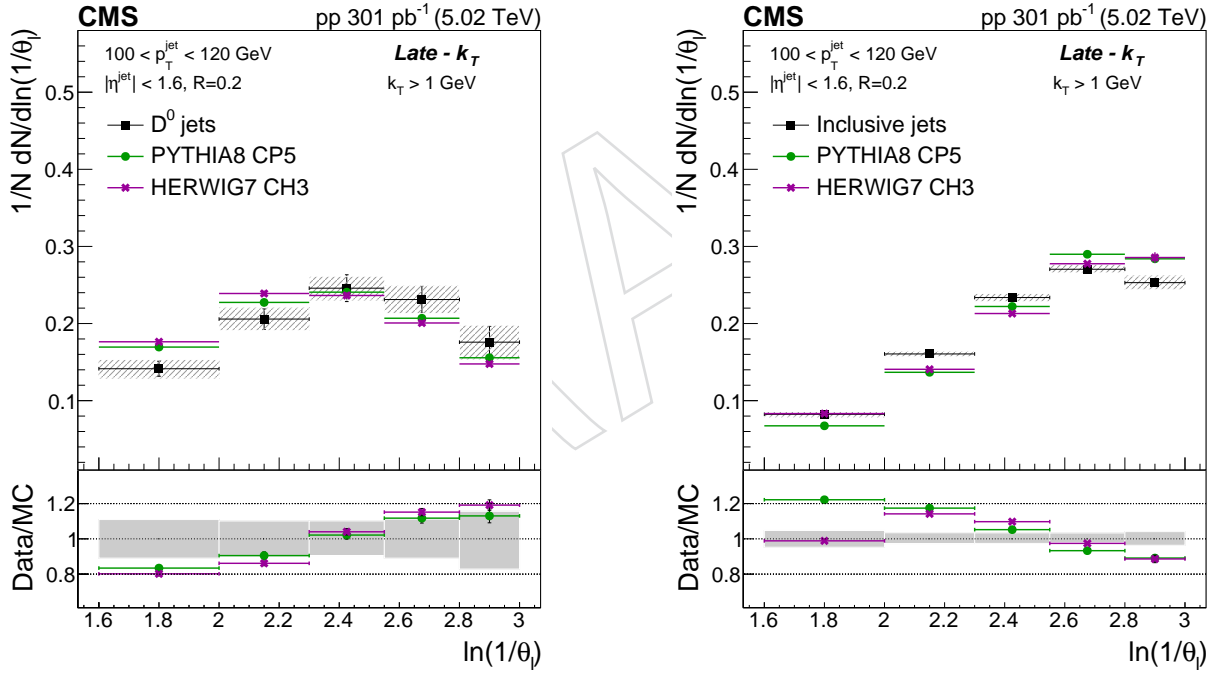

Figure 5: The unfolded late-k_T angular distribution for prompt D^0 jets (left) and inclusive jets (right) compared with predictions from PYTHIA8 CP5 and HERWIG7 CH3. The error bands in the upper panel represent the total systematical uncertainty, whereas the vertical bars represent the statistical uncertainties. In the lower panel, the error band in the ratio plot represents the total experimental uncertainty from the measurement.

Prompt D^0 mesons from gluon splitting to charm quark-antiquark pairs are considered as part of the signal in the analysis. Their impact on the ratio of the distributions of prompt D^0 jets to inclusive jets is studied in PYTHIA8 CP5 and HERWIG7 CH3 generators and shown in Figure 8. Both MC generators allow for the deactivation of gluon splitting to heavy flavor quark-antiquark pairs, which can be used to understand their contribution to the substructure of
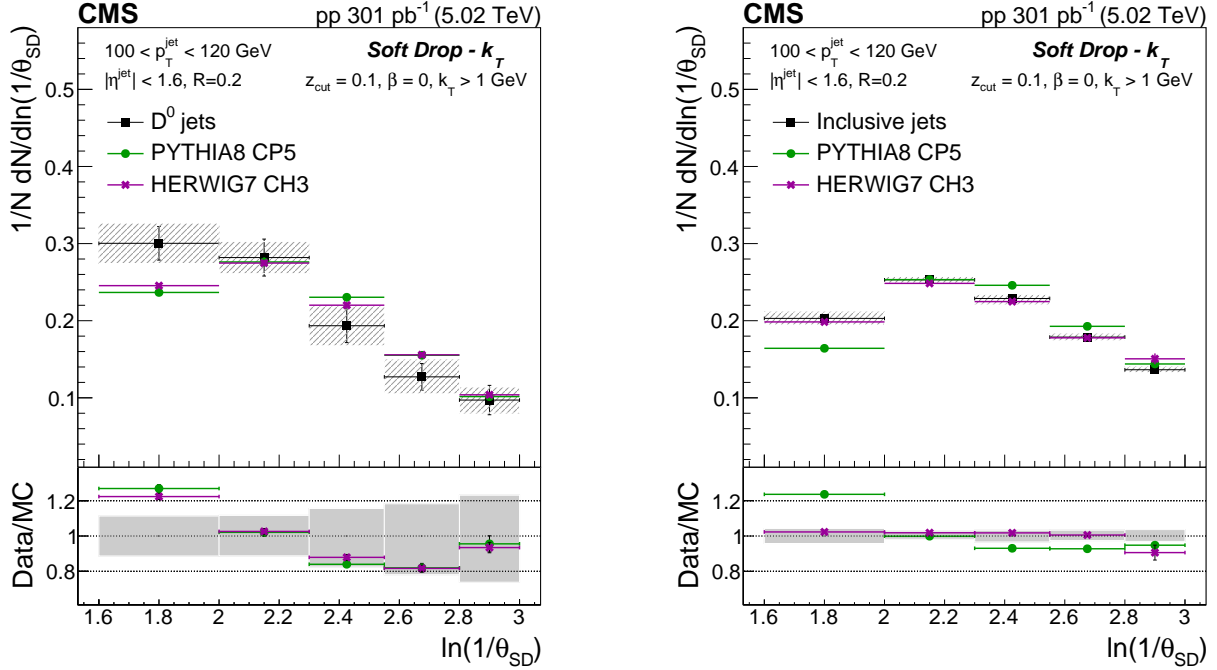
Figure 6: The unfolded soft drop angular distribution for prompt D^0 jets (left) and inclusive jets (right) compared with predictions from PYTHIA8 CP5 and HERWIG7 CH3. The error bands in the upper panel represent the total systematical uncertainty, whereas the vertical bars represent the statistical uncertainties. In the lower panel, the error band in the ratio plot represents the total experimental uncertainty from the measurement.

427 prompt D^0 jets. In Fig. 8, gluon splitting is deactivated only for the prompt D^0 jet distributions.
428 For late-k_T, the gluon splitting contribution is negligible and has an effect mostly at large an-
429 gles. For SD, the gluon splitting direct contribution is stronger and plays a role in the observed
430 shift between the D^0 jet and inclusive jet distributions. This is consistent with the expectation
431 that gluon splitting contributes predominantly at large splitting angles. The emissions found
432 with SD grooming tend to be at larger angles than the ones found by late-k_T algorithm, so the
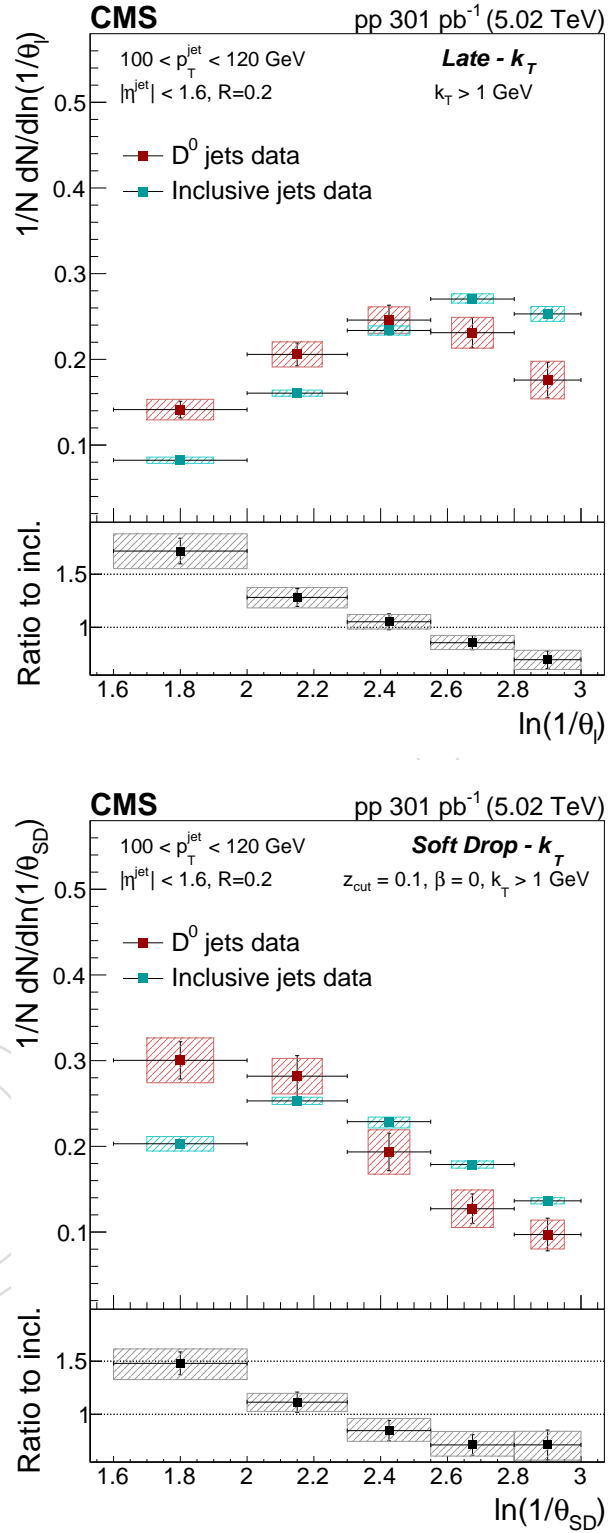433 contribution of gluon splittings is enhanced for SD because of that.

Figure 7: The late-k_T (upper plot) and modified soft drop (lower plot) angular distribution for prompt D^0 jets and inclusive jets. It the lower panels, the ratio to the inclusive jets is shown. The error band represents the total systematic uncertainty, whereas the vertical bars represent the statistical uncertainties.
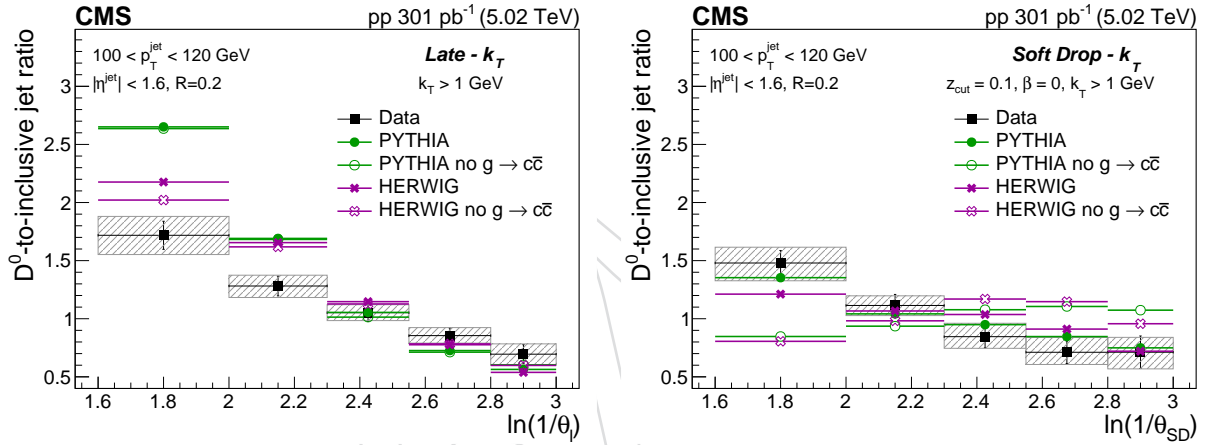
Figure 8: The ratio of the late-k_T angle distributions (left panel) and SD angle (right panel) for prompt D^0 jets to inclusive jets, the data are compared with PYTHIA8 CP5 and HERWIG7 CH3 with and without gluon splitting to charm quark-antiquark pairs.

7 Summary

We have presented a measurement of the substructure of jets containing prompt D^0 mesons and of inclusive jets in proton-proton (pp) collisions at a collision energy of $\sqrt{s} = 5.02$ TeV, corresponding to an integrated luminosity of 301 pb^{-1}, collected in 2017 with the CMS experiment. The analysis focuses on the substructure of jets initially clustered with the anti-k_T algorithm and a distance parameter of $R = 0.2$ with transverse momentum $100 < p_T^{jet} < 120$ GeV and pseudorapidity $|\eta| < 1.6$. Both neutral and charged particles are used for the substructure of these jets. The D^0 meson is identified via its two-pronged decay into a kaon and pion pair.

In this analysis the opening angle between the subjet pair found with two different grooming algorithms that are based on Cambridge–Aachen (CA) reclustering is measured. The angular separation between the two hard subjets found with the soft drop grooming algorithm is studied, using the parameters $z_{cut} = 0.1$ and $\beta = 0$, with the additional requirement that the emission has a minimum relative transverse momentum of $k_T > 1$ GeV. The splitting angle distribution, in this case, is sensitive to contributions from g $\to$ c$\bar{c}$ splitting at large angles and has sensitivity to the dead cone effect for small-angle emissions. The late-k_T grooming algorithm, distinct from the soft drop grooming case, gives access to hard, collinear emissions in an algorithmic way. The late-k_T algorithm consists of selecting the last splitting with a $k_T > 1$ GeV in the CA tree. The resulting angular distribution is more resilient to g $\to$ c$\bar{c}$ splittings and to soft- and wide-angle radiation, and is more sensitive to the dead cone effect. A stronger suppression with respect to the inclusive jet baseline is observed, as expected from the dead cone effect.

This is the first measurement of charm quark jet substructure that probes the hard and collinear region of the jet shower, in a way such that the contribution from hadronization effects is reduced and the connection with the expected parton-level shower is more direct. The jet $p_T > 100$ GeV selection, used for the first time for charm quark jet substructure, increases the phase space available for an interpretation of the jet substructure in terms of perturbation theory calculations. Although the jet p_T is much larger than the charm quark mass, it is possible to isolate hard collinear emissions and observe the suppression due to the charm quark mass in the hard and collinear region.

Acknowledgments

References

[1] ALICE Collaboration, "Direct observation of the dead cone effect in quantum chromodynamics", *Nature* **605** (2022) 440, `doi:10.1038/s41586-022-04572-w`, `arXiv:2106.05713`.

[2] Y. L. Dokshitzer, V. A. Khoze, and S. I. Troian, "On specific QCD properties of heavy quark fragmentation ('dead cone')", *J. Phys. G* **17** (1991) 1602–1604, `doi:10.1088/0954-3899/17/10/023`.

[3] Y. L. Dokshitzer, G. D. Leder, S. Moretti, and B. R. Webber, "Better jet clustering algorithms", *JHEP* **08** (1997) 001, `doi:10.1088/1126-6708/1997/08/001`, `arXiv:hep-ph/9707323`.

[4] L. Cunqueiro and M. Płoskoń, "Searching for the dead cone effects with iterative declustering of heavy-flavor jets", *Phys. Rev. D* **99** (2019), no. 7, 074027, `doi:10.1103/PhysRevD.99.074027`, `arXiv:1812.00102`.

[5] L. Cunqueiro, D. Napoletano, and A. Soto-Ontoso, "Dead cone searches in heavy-ion collisions using the jet tree", *Phys. Rev. D* **107** (2023) 094008, `doi:10.1103/PhysRevD.107.094008`, `arXiv:2211.11789`.

[6] A. J. Larkoski, S. Marzani, G. Soyez, and J. Thaler, "Soft drop", *JHEP* **05** (2014) 146, `doi:10.1007/JHEP05(2014)146`, `arXiv:1402.2657`.

[7] J. M. Butterworth, A. R. Davison, M. Rubin, and G. P. Salam, "Jet substructure as a new Higgs search channel at the LHC", *Phys. Rev. Lett.* **100** (2008) 242001, `doi:10.1103/PhysRevLett.100.242001`, `arXiv:0802.2470`.

[8] ALICE Collaboration, "Measurements of groomed jet substructure of charm jets tagged by D^0 mesons in proton-proton collisions at $\sqrt{s} = 13$ TeV", *Phys. Rev. Lett.* **131** (2023) 192301, `doi:10.1103/PhysRevLett.131.192301`, `arXiv:2208.04857`.

[9] CMS Collaboration, "Luminosity measurement in proton-proton collisions at 5.02 TeV in 2017 at CMS", CMS Physics Analysis Summary CMS-PAS-LUM-19-001, 2021. `http://cds.cern.ch/record/2765655`.

[10] CMS Collaboration, "The CMS experiment at the CERN LHC", *JINST* **3** (2008) S08004, `doi:10.1088/1748-0221/3/08/S08004`.

[11] CMS Collaboration, "Development of the CMS detector for the CERN LHC Run 3", 2023. `arXiv:2309.05466`. Submitted to *JINST*.

[12] CMS Collaboration, "Performance of the CMS Level-1 trigger in proton-proton collisions at $\sqrt{s} = 13$ TeV", *JINST* **15** (2020) P10017, `doi:10.1088/1748-0221/15/10/P10017`, `arXiv:2006.10165`.

[13] CMS Collaboration, "The CMS trigger system", *JINST* **12** (2017) P01020, `doi:10.1088/1748-0221/12/01/P01020`, `arXiv:1609.02366`.

[14] CMS Collaboration, "Electron and photon reconstruction and identification with the CMS experiment at the CERN LHC", *JINST* **16** (2021) P05014, `doi:10.1088/1748-0221/16/05/P05014`, `arXiv:2012.06888`.

[15] CMS Collaboration, "Performance of the CMS muon detector and muon reconstruction with proton-proton collisions at $\sqrt{s} = 13$ TeV", *JINST* **13** (2018) P06015, `doi:10.1088/1748-0221/13/06/P06015`, `arXiv:1804.04528`.

[16] CMS Collaboration, "Description and performance of track and primary-vertex reconstruction with the CMS tracker", *JINST* **9** (2014) P10009, `doi:10.1088/1748-0221/9/10/P10009`, `arXiv:1405.6569`.

[17] CMS Collaboration, "Particle-flow reconstruction and global event description with the CMS detector", *JINST* **12** (2017) P10003, `doi:10.1088/1748-0221/12/10/P10003`, `arXiv:1706.04965`.

[18] CMS Collaboration, "Performance of reconstruction and identification of τ leptons decaying to hadrons and ν_τ in pp collisions at $\sqrt{s} = 13$ TeV", *JINST* **13** (2018) P10005, `doi:10.1088/1748-0221/13/10/P10005`, `arXiv:1809.02816`.

[19] CMS Collaboration, "Jet energy scale and resolution in the CMS experiment in pp collisions at 8 TeV", *JINST* **12** (2017) P02014, `doi:10.1088/1748-0221/12/02/P02014`, `arXiv:1607.03663`.

[20] CMS Collaboration, "Performance of missing transverse momentum reconstruction in proton-proton collisions at $\sqrt{s} = 13\,\text{TeV}$ using the CMS detector", *JINST* **14** (2019) P07004, `doi:10.1088/1748-0221/14/07/P07004`, `arXiv:1903.06078`.

[21] M. Cacciari, G. P. Salam, and G. Soyez, "The anti-k_T jet clustering algorithm", *JHEP* **04** (2008) 063, `doi:10.1088/1126-6708/2008/04/063`, `arXiv:0802.1189`.

[22] M. Cacciari, G. P. Salam, and G. Soyez, "FastJet user manual", *Eur. Phys. J. C* **72** (2012) 1896, `doi:10.1140/epjc/s10052-012-1896-2`, `arXiv:1111.6097`.

[23] H. A. Andrews et al., "Novel tools and observables for jet physics in heavy-ion collisions", *J. Phys. G* **47** (2020) 065102, `doi:10.1088/1361-6471/ab7cbc`, `arXiv:1808.03689`.

[24] CMS Collaboration, "Determination of jet energy calibration and transverse momentum resolution in CMS", *JINST* **6** (2011) P11002, `doi:10.1088/1748-0221/6/11/P11002`, `arXiv:1107.4277`.

[25] Particle Data Group Collaboration, "Review of Particle Physics", *PTEP* **2022** (2022) 083C01, `doi:10.1093/ptep/ptac097`.

[26] H. Voss, A. Höcker, J. Stelzer, and F. Tegenfeldt, "TMVA, the toolkit for multivariate data analysis with ROOT", in *XIth International Workshop on Advanced Computing and Analysis Techniques in Physics Research (ACAT)*, p. 40. 2007. `arXiv:physics/0703039`. [PoS(ACAT)040]. `doi:10.22323/1.050.0040`.

[27] T. Sjöstrand et al., "An introduction to PYTHIA8.2", *Comput. Phys. Commun.* **191** (2015) 159, `doi:10.1016/j.cpc.2015.01.024`, `arXiv:1410.3012`.

[28] CMS Collaboration, "Extraction and validation of a new set of CMS PYTHIA8 tunes from underlying event measurements", *Eur. Phys. J. C* **80** (2020) 4, `doi:10.1140/epjc/s10052-019-7499-4`, `arXiv:1903.12179`.

[29] S. Gieseke, P. Stephens, and B. Webber, "New formalism for QCD parton showers", *JHEP* **12** (2003) 045, `doi:10.1088/1126-6708/2003/12/045`, `arXiv:hep-ph/0310083`.

[30] NNPDF Collaboration, "Parton distributions for the LHC Run 2", *JHEP* **04** (2015) 040, `doi:10.1007/JHEP04(2015)040`, `arXiv:1410.8849`.

[31] B. R. Webber, "A QCD model for jet fragmentation including soft gluon interference", *Nucl. Phys. B* **238** (1984) 492, `doi:10.1016/0550-3213(84)90333-X`.

[32] CMS Collaboration, "Development and validation of HERWIG7 tunes from CMS underlying event measurements", *Eur. Phys. J. C* **81** (2021) 312, `doi:10.1140/epjc/s10052-021-08949-5`, `arXiv:2011.03422`.

[33] GEANT4 Collaboration, "GEANT4—a simulation toolkit", *Nucl. Instrum. Meth. A* **506** (2003) 250, `doi:10.1016/S0168-9002(03)01368-8`.

[34] P. Skands, S. Carrazza, and J. Rojo, "Tuning PYTHIA8.1: the Monash 2013 tune", *Eur. Phys. J. C* **74** (2014) 3024, `doi:10.1140/epjc/s10052-014-3024-y`, `arXiv:1404.5630`.

[35] CMS Collaboration, "Event generator tunes obtained from underlying event and multiparton scattering measurements", *Eur. Phys. J. C* **76** (2016) 155, `doi:10.1140/epjc/s10052-016-3988-x`, `arXiv:1512.00815`.

[36] M. Wobisch and T. Wengler, "Hadronization corrections to jet cross sections in deep inelastic scattering", in *Workshop on Monte Carlo generators for HERA physics*, p. 270. 1998. `arXiv:hep-ph/9907280`. `doi:10.48550/arXiv.hep-ph/9907280`.

[37] S. Caletti, A. Ghira, and S. Marzani, "On heavy-flavor jets with soft drop", *Eur. Phys. J. C* **84** (2024) 212, `doi:10.1140/epjc/s10052-024-12562-7`, `arXiv:2312.11623`.

[38] G. D'Agostini, "A multidimensional unfolding method based on Bayes' theorem", *Nucl. Instrum. Meth. A* **362** (1995) 487, `doi:10.1016/0168-9002(95)00274-X`.

[39] T. Adye, "Unfolding algorithms and tests using RooUnfold", in *PHYSTAT 2011 Workshop on Statistical Issues Related to Discovery Claims in Search Experiments and Unfolding*, H. Prosper and L. Lyons, eds., p. 313. Geneva, Switzerland, 2011. `arXiv:1105.1160`. `doi:10.5170/CERN-2011-006.313`.

[40] CMS Collaboration, "Single-particle response in the CMS calorimeters", CMS Physics Analysis Summary CMS-PAS-JME-10-008, 2010.

[41] CMS Collaboration, "Measurements of azimuthal anisotropy of nonprompt D^0 mesons in PbPb collisions at 5.02TeV", *Phys. Lett. B* **850** (2024) 138389, `doi:10.1016/j.physletb.2023.138389`, `arXiv:2212.01636`.

[42] CMS Collaboration, "Study of quark and gluon jet substructure in Z+jet and dijet events from pp collisions", *JHEP* **01** (2022) 188, `doi:10.1007/JHEP01(2022)188`, `arXiv:2109.03340`.

[43] CMS Collaboration, "Measurement of the primary Lund jet plane density in proton-proton collisions at $\sqrt{s} = 13$ TeV", *JHEP* **05** (2024) 116, `doi:10.1007/JHEP05(2024)116`, `arXiv:2312.16343`.